Journal of Solid State Electrochemistry (2021) 25:1657–1665
https://doi.org/10.1007/s10008-021-04936-8

ORIGINAL PAPER

Carbon-encapsulated nanosphere-assembled MoS_2 nanosheets with large interlayer distance for flexible lithium-ion batteries

Zuxue Bai[1] · Ya Yang[1] · Deyang Zhang[1] · Yangbo Wang[1] · Ying Guo[1] · Hailong Yan[1] · Paul K. Chu[3] · Yongsong Luo[1,2]

Received: 20 January 2021 / Revised: 28 February 2021 / Accepted: 1 March 2021 / Published online: 8 March 2021

Abstract

2D transition metal dichalcogenides such as MoS_2 with the unique layered structure have received great attention in the field of lithium-ion batteries (LIBs). However, the low conductivity and poor structural stability adversely affect the rate performance of LIBs. Herein, a flexible and free-standing high-performance lithium-ion battery electrode (MoS_2/C@$Ti_3C_2T_x$) composed of rice-candy-like MoS_2/C intercalated $Ti_3C_2T_x$ and PVP-derived carbon with a large interlayer distance of MoS_2 is designed and demonstrated. Lithium-ion batteries have attracted great attention due to their high energy density. Consequently, as an anode material for lithium-ion batteries, MoS_2/C@$Ti_3C_2T_x$ provides a high discharge capacity of 538.5 mAh g^{-1} at 0.05 A g^{-1} and rapid charge/discharge capability of 256.7 mAh g^{-1} at 2 A g^{-1}, as well as outstanding cycling property (96.7% capacity retention after 150 cycles at 2 A g^{-1}). Density-functional theory (DFT) calculation reveals that the rice-candy-like MoS_2/C structure favors adsorption and diffusion of lithium ions and facilitates the redox reactions. The MoS_2/C@$Ti_3C_2T_x$ structure is expected to boost the development of novel 2D materials for high-performance lithium-ion batteries.

Keywords Lithium-ion battery · MoS_2 · $Ti_3C_2T_x$ · Large interlayer distance · Flexible electrode

Introduction

Lithium-ion batteries (LIBs) boasting many advantages such as large energy density, long-term cycle life, and environmental friendliness are widely used in portable electronics and electric vehicles [1–3]. As a class of 2D materials, molybdenum disulfide (MoS_2) with a graphene-like layered structure has attracted attention in physics and chemistry [4, 5]. The layered structure composed of S–Mo–S units stacked by van der Waals attraction [6–8] has a large theoretical specific capacity of 670 mAh g^{-1} for Li-ion batteries [9–11]. However, commercial adoption of MoS_2 is hampered by the low electrical properties, which limit ion and electron transport [12], large volume variation during adsorption and diffusion of lithium ions [13], and polysulfide dissolution during charging and discharging [14]. To overcome these hurdles, efforts have been made to design nanoscale structures of MoS_2 and MoS_2/carbon composites such as MoS_2 nanosheets [15, 16], MoS_2/graphene [17, 18], and MoS_2/CNT composites [19, 20]. In fact, MoS_2 with large interlayer spacing and abundant active sites increases the diffusion coefficient of Li^+ and enhances the battery performance [21–23]. For example, Jing et al. fabricated 1–3 layers MoS_2 with wide spacing by lithiation-exfoliation process; the LIB shows a rate capacity of 350 mAh g^{-1} at 0.5 A g^{-1} and the coulombic efficiency only 52% at the first cycle [24]. Hence, expansion of the interlayer distance can be realized by introducing carbon materials during the synthesis of MoS_2 to improve storage of lithium ions.

Zuxue Bai and Yangbo Wang contributed equally to this work.

✉ Deyang Zhang
zdy@xynu.edu.cn

✉ Yongsong Luo
ysluo@xynu.edu.cn

[1] Key Laboratory of Microelectronics and Energy of Henan Province, School of Physics and Electronic Engineering, Engineering Research Center for MXene Energy Storage Materials of Henan Province, Xinyang Normal University, Xinyang 464000, People's Republic of China

[2] College of Physics and Electronic Engineering, Nanyang Normal University, Nanyang 473061, People's Republic of China

[3] Department of Physics, Department of Materials Science & Engineering, and Department of Biomedical Engineering, City University of Hong Kong, Tat Chee Avenue, Kowloon, Hong Kong, China

Recently, MXene (e.g., $Ti_3C_2T_x$, V_2CT_x, and Ti_2CT_x) as a new candidate of two-dimensional materials has attracted extensive attention in energy storage devices. MXenes are also described as $M_{n+1}X_nT_x$, where M stands for early transition metal. X represents a carbon or nitrogen element. T_x is the surface chemical groups. MXene, a promising material for LIBs with more unique properties than graphene or other 2D materials, has been regarded as a potential material for electrochemical energy storage because of its layered structure and excellent conductivity. For example, Qiu et al. fabricated few-layered MoS_2 nanoplates on $Ti_3C_2T_x$ nanosheets stabilized by a carbon layer, which exhibited outstanding electrochemical performance for lithium storage [25]. Fabrication of MXene hybrid nanostructures with other materials is a well-known method, which can be utilized for important applications including supercapacitors [26] and sensors [27, 28]. Yola et al. prepared MWCNTs with $Ti_3C_2T_x$ (mass ratio 3:1) colloidal solution, which exhibited high sensitivity of electrochemistry [29]. Therefore, these characteristics make $Ti_3C_2T_x$ a suitable candidate for the base material to construct excellent performance MoS_2 nanohybrid anode materials for lithium-ion storage.

In the present work, rice-candy-like MoS_2 is mixed with $Ti_3C_2T_x$ to form the self-supporting composite film of $MoS_2/C@Ti_3C_2T_x$ by vacuum filtration. The sandwiched structure of free-standing $MoS_2/C@Ti_3C_2T_x$ offers many advantages. It solves the stacking problem of $Ti_3C_2T_x$ and MoS_2 and dynamically enhances Li^+ transport. Moreover, the free-standing $MoS_2/C@Ti_3C_2T_x$ electrode buffers the volume change and avoids fast capacity decay at high charging/discharging rates. The key for $MoS_2/C@Ti_3C_2T_x$ is that PVP-derived carbon is encapsulated on the MoS_2 layer, so that diffusion of lithium ions is facilitated and the volume variation of MoS_2 in charging and discharging is buffered. Consequently, the flexible $MoS_2/C@Ti_3C_2T_x$ exhibits higher reversible capacity and better cycling stability than $MoS_2@Ti_3C_2T_x$. Density-functional theory (DFT) calculation proves that the large interlayer distance enhances the lithium storage capacity.

Experimental

Sample preparation

Synthesis of Ti_3AlC_2

Ti, Al, and TiC powders with a molar ratio of 1:1.1:2 were mixed for 12 h by the ball mill method, and Ti_3AlC_2 was prepared by spark plasma sintering (SPS, 211HF) at 1400 °C for 20 min at a pressure of 20 MPa under vacuum. The Ti_3AlC_2 monolith was milled and sieved to obtain 400 mesh Ti_3AlC_2 powder.

Preparation of $Ti_3C_2T_x$

The $Ti_3C_2T_x$ solution was prepared by selective etching of the Ti_3AlC_2 powder. Typically, 1 g of LiF was immersed in 20 mL of 9 M HCl and stirred magnetically until LiF dissolved completely at 35 °C. One gram of Ti_3AlC_2 was introduced and stirred vigorously at 35 °C for 12 h. Afterwards, the precipitate was rinsed with deionized water several times until the pH was approximately 6. The sediment was dispersed in 150 mL of DI water and sonicated for 60 min under flowing Ar. After centrifugation at 3500 rpm for 60 min, the dark green supernatant of $Ti_3C_2T_x$ was collected.

Synthesis of MoS_2/C

A total of 0.1 g of ammonium molybdate, 0.09 g of thiourea, and 0.41 g of polyvinyl pyrrolidone were dissolved in 30 mL of DI water under magnetic stirring and transferred to a Teflon-lined stainless steel autoclave (50 mL) which was heated to 190 °C for 18 h in an electric oven. After natural cooling to room temperature, the MoS_2/C composite material was gathered by centrifugation, washed with DI water and anhydrous ethanol several times, and then freeze-dried for 12 h. The MoS_2/C composite was then heat-treated at 500 °C for 3 h under Ar. The MoS_2 composite was prepared by the same method but without adding PVP.

Fabrication of the flexible $MoS_2/C@Ti_3C_2T_x$ film

The diluted aqueous dispersion (1 mg mL^{-1}) of MoS_2/C was prepared by sonication for 30 min. It was introduced to the $Ti_3C_2T_x$ solution (0.04 g, 2 mg mL^{-1}) and stirred magnetically. The total volume of the solution was 40 mL with the $Ti_3C_2T_x$:MoS_2/C ratio of 2:3. After vacuum filtration, the membrane was freeze-dried for 9 h. The flexible $MoS_2/C@Ti_3C_2T_x$ film was gathered by peeling from the filter membrane and used directly as an anode for the LIBs. As a reference, the $MoS_2@Ti_3C_2T_x$ film was also produced by the same procedure.

Materials characterization

X-Ray diffraction was performed on the D2-Advance (Bruker) automated X-ray diffractometer with Cu K_α radiation (λ = 1.5418 Å), and the STA449F5 (NETZSCH) was employed in the thermogravimetric (TG) analysis from 20 to 800 °C at 10 °C min^{-1} at an oxygen flow rate of 100 mL min^{-1}. Field-emission scanning electron microscopy (FESEM, JEOL S-4800, 10 kV) and transmission electron microscopy (TEM, Tecnai G2 F20) were carried out to examine the structure of the $MoS_2/C@Ti_3C_2T_x$ film. X-Ray photoelectron spectroscopy was characterized on the K-ALPHA 0.5 eV with monochromatic Al K_α radiation, and Raman

scattering was investigated by the INVIA Raman microprobe (Renishaw Instruments) with a 532-nm laser source.

Electrochemical measurements

A lithium foil was utilized for the counter electrode in the 2032-type coin cell, and the electrolyte was 1 M $LiPF_6$ in a mixture of ethylene carbonate (EC):diethylene carbonate (DEC) (1:1 by volume). Assembly was carried out in an argon-filled glovebox. Electrochemical impedance spectroscopy (EIS) was performed in the frequency range from 0.01 Hz to 100 kHz with a potentiostatic signal amplitude of 5 mV. Cyclic voltammetry (CV) was tested on a VMP3 electrochemical workstation at different scanning rates, and galvanostatic charge-discharge experiments were measured using the Neware battery testing system with the voltage range of 0.01–3 V (vs Li/Li^+).

Theoretical calculation

First-principles calculation was performed by the Perdew-Burke-Ernzerhof (PBE) exchange-correlation functional within the general gradient approximation (GGA) using the VASP code and considering all the spin-polarized calculation. The geometric structure was relaxed until the Feynman force on each atom was less than 0.01 eV/Å. The energy was optimized until the convergence condition was less than 10^{-5} eV. Considering the van der Waals interactions, the DFT-D2 approach was adopted in the dispersion correction. The 3 × 3 and 4 × 4 supercells of MoS_2/C were chosen as the substrate for the bilayer MoS_2, and the G sandwiched structure was adopted. The c axis vacuum was set as 15 Å to avoid interactions between slabs. The plane wave cutoff energy was 450 eV. A k-points mesh of 3 × 3 × 1 in the gamma-center sampling scheme was used for geometry optimization and electronic self-consistency.

Results and discussion

The fabrication procedures of the flexible MoS_2/C@$Ti_3C_2T_x$ film are illustrated in Fig. 1. $Ti_3C_2T_x$ nanosheets are synthesized by selectively etching the Al layer from Ti_3AlC_2. Using ammonium molybdate as the molybdenum source, thiourea as the sulfur source, and PVP as the carbon source, carbon-encapsulated nanosphere-assembled MoS_2 nanosheets are prepared by a hydrothermal reaction and annealing at 500 °C under flowing Ar. The sandwiched structure of MoS_2/C@$Ti_3C_2T_x$ flexible film was synthesized by vacuum filtration and freeze-drying.

The homogeneous MoS_2/C@$Ti_3C_2T_x$ solution is the key to the preparation of the flexible film. Figure S1a displays the Tyndall effect of the $Ti_3C_2T_x$ solution, and after mixing the rice-candy-like MoS_2/C solution with the $Ti_3C_2T_x$ solution under vigorous stirring, a well-dispersed MoS_2/C@$Ti_3C_2T_x$ solution is obtained as verified by the Tyndall effect as shown in Fig. S1b [30]. The X-ray diffraction (XRD) patterns of Ti_3AlC_2, $Ti_3C_2T_x$, MoS_2/C, and MoS_2 in Fig. 2a and b reveal the presence of Ti_3AlC_2. After etching and delamination, the sharp diffraction peak at 9.5° disappears but a new peak arising from the (002) plane of $Ti_3C_2T_x$ is observed at 7° further confirming successful delaminate of the $Ti_3C_2T_x$ nanosheets [31]. The XRD pattern of MoS_2 in Fig. 2b can be indexed to the JCPDS card (37-1492) with a d (002) spacing of 0.615 nm. The sharp diffraction peak at 14.378° indicates that MoS_2 is made of a single or a few layers assembled by van der Waals attraction [32]. Although the 14.375° diffraction peaks of MoS_2 cannot be observed from MoS_2/C@$Ti_3C_2T_x$, there are two diffraction peaks at 6.584° and 12.93° corresponding to interlayer distances of 13.41 Å and 6.84 Å, respectively, indicating that the large interlayer distance of 0.67 nm for the PVP-derived carbon layer is combined into the two MoS_2 interlayers. The calculation shows it is the middle spacing of the MoS_2 interlayer distance [33]. The XRD result of MoS_2/C@$Ti_3C_2T_x$ is presented in Fig. S2. As displayed in Fig. S3, The E^1_{2g} (381.68 cm^{-1}) and A_{1g} (404.78 cm^{-1}) peaks correspond to the in-plane vibration of Mo and S atoms and the out-of-plane vibration of S atoms, respectively. The separation (Δk) of MoS_2/C is 23.1 cm^{-1}, which smaller than 27.4 cm^{-1} of MoS_2 [33, 34]. The Δk is positively correlated with the layer number, which increases with the layer number. From the Raman Spectroscopy, it can be concluded the MoS_2/C not only has a less number of layers, but also has a large interlayer distance than MoS_2. The content of PVP-derived carbon is calculated by Eq. (1) based on the thermogravimetric analysis (TGA) in an oxygen atmosphere:

$$MoS_2(\mathrm{wt}\%) = \frac{a}{b} \times c \times 100\% \quad (1)$$

where a is the molecular weight of MoS_2, b is the molecular weight of MoO_3, and c is the total residual weight. According to the TG analysis (Fig. 2c), the PVP-derived carbon concentration is 25.69%.

Figure 2d exhibits the presence of Ti, C, Mo, S, and O, and the elemental composition is listed in Table S1. Figure 2e can be deconvoluted into three peaks: 455.1 and 461.1 eV for Ti-C, 455.6 and 462 eV for Ti^{2+}, 456.4 eV for Ti^{3+}, 457.5 eV for Ti-O, 458.9 eV for Ti-F [35–38]. Figure 2f shows that the peaks at 281.9 eV, 284.6 eV, and 286.2 eV are related to C-Ti, C-C, and C-O, respectively [39], and Fig. 2g shows that the peaks at 529.6 eV, 531.8 eV, 532.2 eV, and 533.1 eV are related to O-Ti, O-Ti/OH, O-C/OH, and H_2O, respectively [40]. As shown in Fig. 2h and i, the Mo 3d spectra of MoS_2/C@$Ti_3C_2T_x$ exhibiting three main peaks at 229.4 eV, 232.6 eV, and 225.8 eV are assigned to Mo $3d_{5/2}$, Mo $3d_{3/2}$, and Mo^{4+}. The S $2p_{1/2}$ and S $2p_{3/2}$ peaks in the S 2p spectrum are at 162.4 and 161.3 eV, respectively [41].

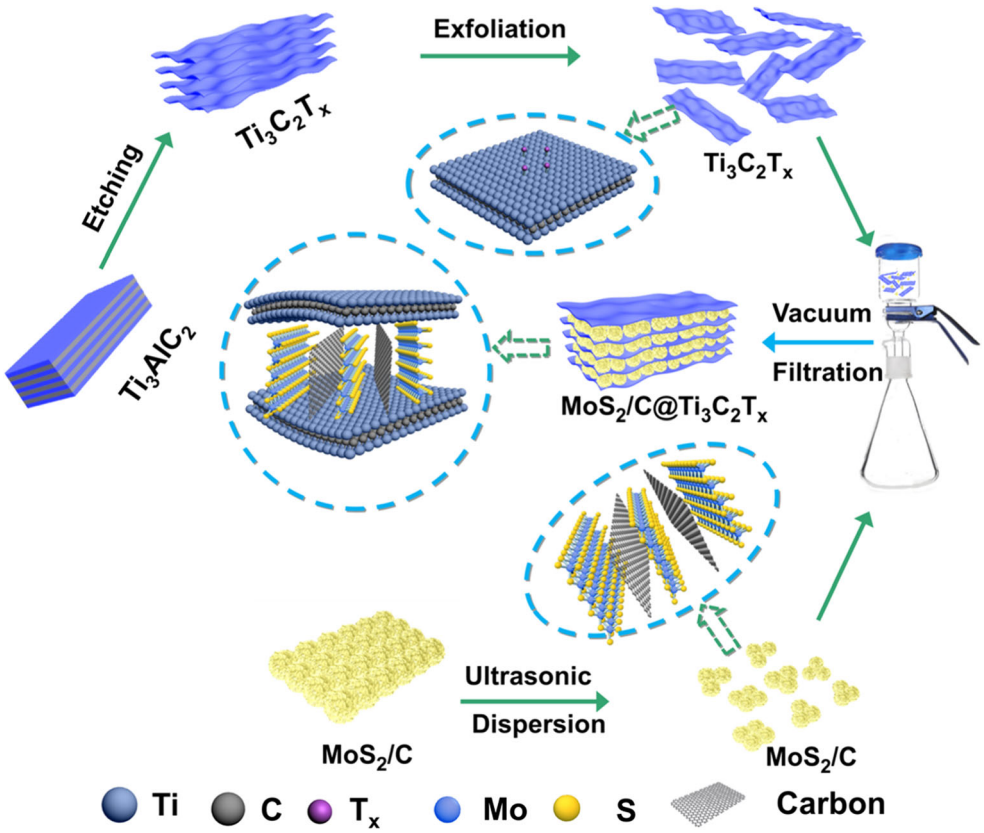

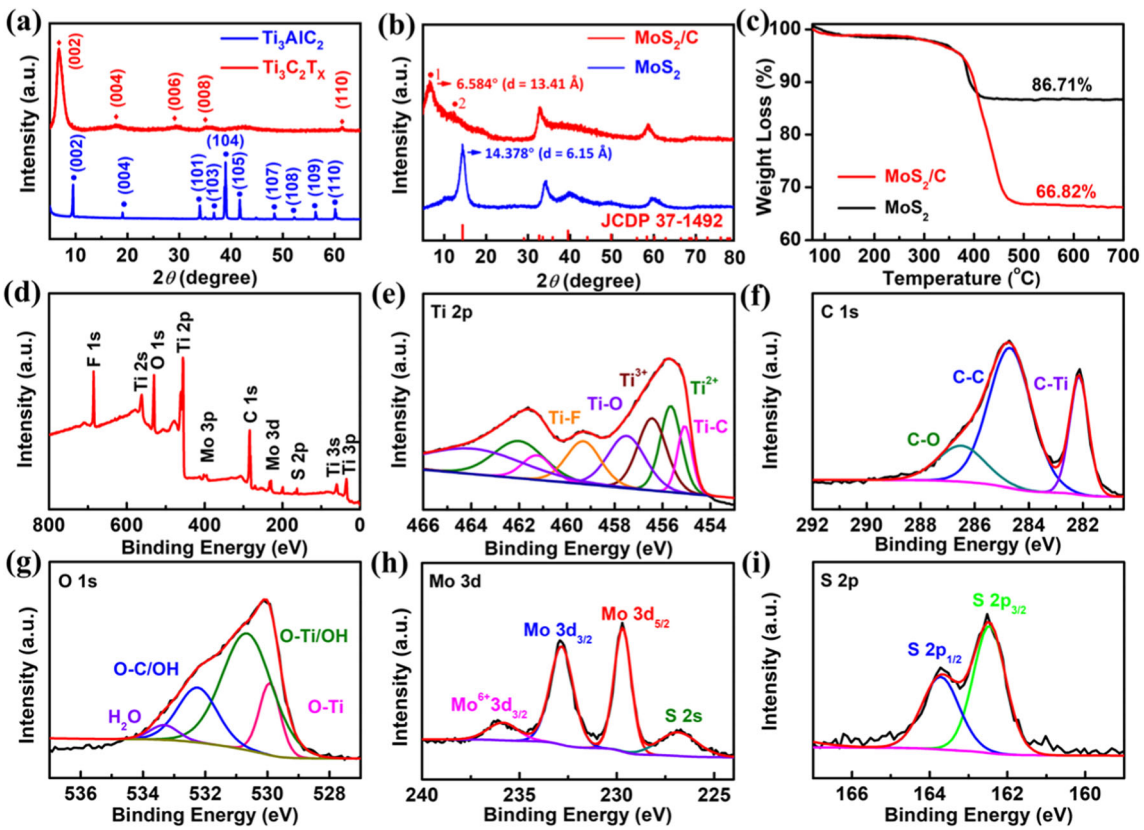

Fig. 1 Schematic illustration of the fabrication process of MoS_2/C@$Ti_3C_2T_x$ flexible electrode

Fig. 2 **a** XRD patterns of the Ti_3AlC_2 and $Ti_3C_2T_x$. **b** XRD patterns of the MoS_2/C and MoS_2. **c** TGA curves of MoS_2/C and MoS_2. **d** XPS survey scan spectra. **e** Ti 2p, **f** C 1s, **g** O 1s, **h** Mo 3d, and **i** S 2p of MoS_2/C@$Ti_3C_2T_x$ spectra

The morphology of the Ti_3AlC_2, $Ti_3C_2T_x$, MoS_2/C@$Ti_3C_2T_x$, and MoS_2@$Ti_3C_2T_x$ is observed by SEM and TEM. The SEM image shows that the pristine Ti_3AlC_2 powder has a slightly layered texture but it appears to be seamless (Fig. S4a). The flake-shape folded structure in Fig. S4b corroborates successful synthesis of $Ti_3C_2T_x$ nanosheets. After vacuum filtration of the $Ti_3C_2T_x$ suspension, a flexible film is produced as shown in Fig. S4c. The TEM image of $Ti_3C_2T_x$ in Fig. S4d reveals the flexible characteristic, and Fig. 3a shows that the MoS_2/C nanosheets and $Ti_3C_2T_x$ are well-dispersed together with the sandwiched structure of $Ti_3C_2T_x$ and MoS_2/C. The inset in Fig. 3a is the digital photograph of the MoS_2/C@$Ti_3C_2T_x$ film and the magnified image is in Fig. 3b. The MoS_2 nanosphere/carbon hybrid has a nanosheet morphology resembling rice candies (Fig. 3c).

The high-resolution TEM (HR-TEM) image in Fig. 3d shows that the MoS_2/C nanospheres consist of layered nanoflakes. The interlayer spacing of the MoS_2/C (002) plane is 13.41 Å, which is much larger than that of the MoS_2 (002) plane of 6.2 Å as shown in Fig. 3e and f. This result is in accordance with the above XRD calculations. Figure S5a and 5b show that MoS_2 are single nanospheres. Figure 3g shows dense and sparse contrast difference suggesting some overlapping of Ti, C, Mo, and S. Furthermore, in the MoS_2/C@$Ti_3C_2T_x$ structure, Mo, S, and C are concentrated in the MoS_2/C nanoflakes and Ti overlaps along the folded $Ti_3C_2T_x$, providing evidence that the MoS_2/C nanoflakes are mixed uniformly with the flake-shaped folded $Ti_3C_2T_x$ nanosheets. It can be concluded that PVP-derived carbon is intercalated into MoS_2 to expand the interlayer distance. The abundant active sites and rapid Li^+ diffusion arise from the larger interlayer distance and PVP-derived carbon.

The lithium storage property of the flexible MoS_2/C@$Ti_3C_2T_x$ is determined from lithium-ion half-cells. Figure 4a presents the first three cycles of the cyclic voltammetry (CV) curves of the MoS_2/C@$Ti_3C_2T_x$ flexible electrode at 0.1 mV s^{-1}. In the first cathodic scan, three reduction peaks at 0.8 V, 0.5 V, and 0.2 V can be seen. The first one (0.8 V) represents intercalation of Li^+ insertion into MoS_2 to form Li_xMoS_2 [42], and the other two peaks (0.5 and 0.2 V) are attributed to reduction of Li_xMoS_2 to metallic Mo and Li_2S by the conversion reaction and creation of a solid electrolyte interphase (SEI) layer on the electrode [43]. In addition, anodic peaks appear at 1.3 V and 2.3 V corresponding to partial oxidation of Mo to MoS_2 and Li_2S to S, respectively. In the subsequent cathodic scan, the peak at 1.2 V is related to the conversion of MoS_2 into Mo and that at 1.9 V is related to the formation of Li_2S [44]. As shown in Fig. 4b, the galvanostatic discharge/charge curves of the flexible MoS_2/C@$Ti_3C_2T_x$ electrode at 0.05 A g^{-1} over the range between 0.01 V and 3.0 V deliver initial discharge and charge capacities of 733 and 597 mAh g^{-1}, respectively, in conjunction with an initial

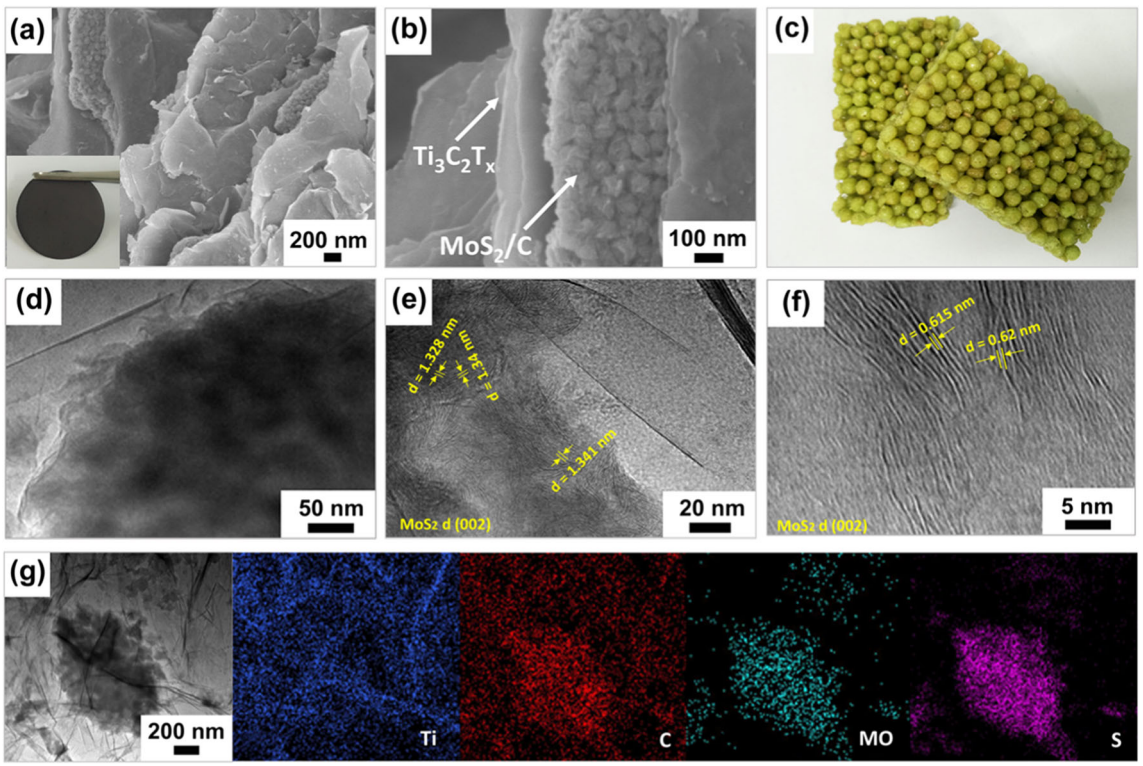

Fig. 3 **a**, **b** SEM images of the MoS_2/C@$Ti_3C_2T_x$ at different magnifications. **c** The digital photographs of crunchy-rice candy, **d** TEM images, and **e** HRTEM image of MoS_2/C@$Ti_3C_2T_x$. **f** HRTEM image of MoS_2@$Ti_3C_2T_x$. **g** Corresponding mapping images for Ti, C, Mo, and S elements of MoS_2/C@$Ti_3C_2T_x$

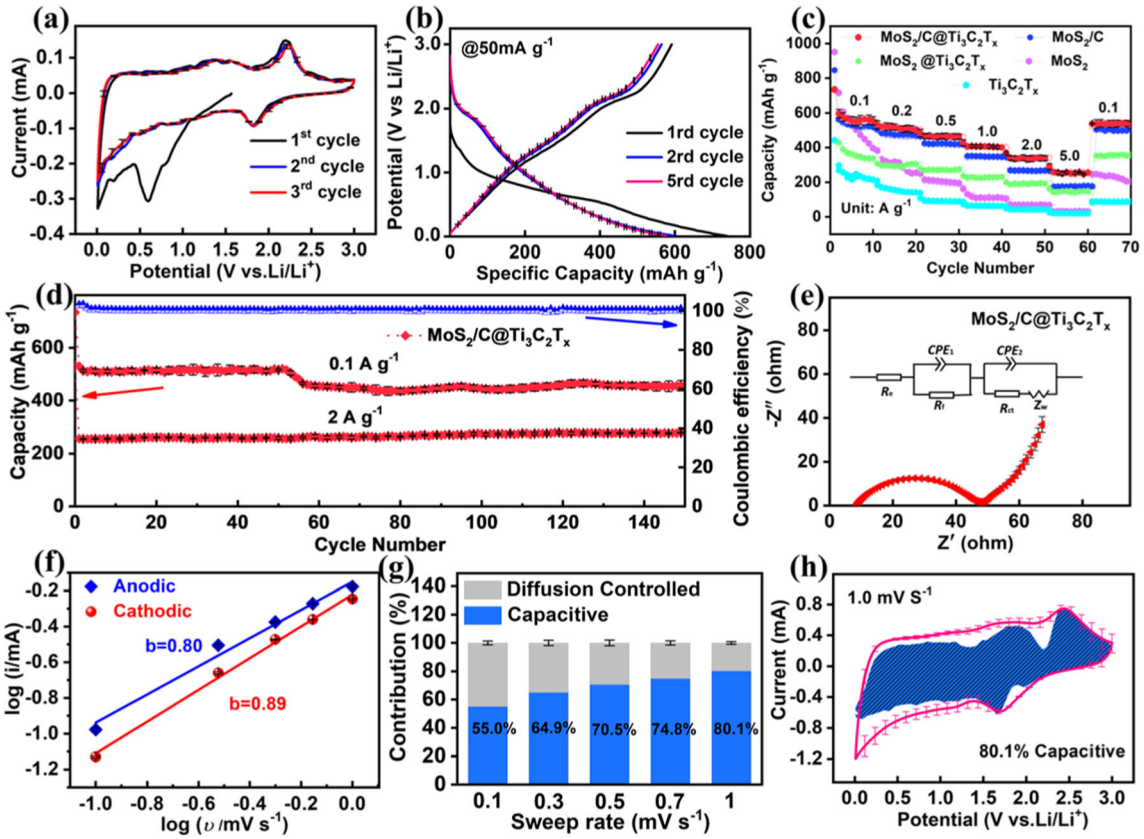

Fig. 4 **a** CV curves of $MoS_2/C@Ti_3C_2T_x$ at 0.1 mV s^{-1}. **b** Galvanostatic discharge/charge curves of the $MoS_2/C@Ti_3C_2T_x$ electrode at 50 mA g^{-1}. **c** Rate capability of the $MoS_2/C@Ti_3C_2T_x$, $MoS_2/Ti_3C_2T_x$, MoS_2/C, MoS_2, and $Ti_3C_2T_x$ electrode at various current densities. **d** Long-term cycling performance of the $MoS_2/C@Ti_3C_2T_x$ and $MoS_2@Ti_3C_2T_x$ at 0.1 A g^{-1} and 2 A g^{-1}. **e** Nyquist plots of the $MoS_2/C@Ti_3C_2T_x$ electrode. **f** *b* values determined by the plot of log (*i*) versus log (*υ*). **g** Normalized ratio of pseudocapacitive and diffusion-controlled contribution of the $MoS_2/C@Ti_3C_2T_x$ at different sweep rates. **h** Capacitive contribution at 1.0 mV s^{-1}

coulombic efficiency of 81.4%. The irreversible capacity loss in the first cycle can be attributed to the formation of the irreversible SEI film. In subsequent cycles, the discharge/charge capacity is quite similar, illustrating the high reversibility in the electrochemical reactions.

A comparison of the rate and cycling performance of the $MoS_2/C@Ti_3C_2T_x$, $MoS_2@Ti_3C_2T_x$, MoS_2/C, MoS_2, and $Ti_3C_2T_x$ samples at different various current densities is shown in Fig. 4c. As expected, the flexible $MoS_2/C@Ti_3C_2T_x$ electrode exhibits excellent rate capabilities of 538.5, 510.5, 461.8, 405.6, 337.7, and 256.7 mAh g^{-1} at 0.05, 0.1, 0.2, 0.5, 1, and 2 A g^{-1}, respectively. When the current density rises again to 0.05 A g^{-1}, the discharge capacity of 538 mAh g^{-1} can be restored rapidly implying remarkable reversibility. In addition, the long cycling stability of the flexible $MoS_2/C@Ti_3C_2T_x$ electrode is assessed. Figure 4d shows the cycling performances at current densities of 0.1 A g^{-1} and 2 A g^{-1}; the retain capacities of 489.3 and 248.4 mA h g^{-1} are observed after 150 cycles, respectively. The excellent rate performance of $MoS_2/C@Ti_3C_2T_x$ mainly ascribed to PVP-derived carbon is intercalated into MoS_2 to expand the interlayer distance, and dynamically facilitates electron/ion transport. Apparently, the result indicates that the ultra-wide interlayer spacing MoS_2 and $Ti_3C_2T_x$ flexible film could dramatically enhance lithium storage capacity as expected. Compared with other 2D materials for LIBs, the as-prepared $MoS_2/C@Ti_3C_2T_x$ shows a high rate performance (Table S2). Figure S6 depicts the cross-sectional SEM image of $MoS_2/C@Ti_3C_2T_x$ after 150 cycles at 0.1 A g^{-1}, and $MoS_2/C@Ti_3C_2T_x$ retains the sandwiched morphology confirming the good structural stability. Therefore, the superior rate performance of $MoS_2/C@Ti_3C_2T_x$ is mainly attributed to the larger interlayer distance of MoS_2 and the high electrical conductivity of $Ti_3C_2T_x$.

To further confirm the impact of PVP-derived carbon, the Nyquist plots of the flexible electrodes are shown in Fig. 4e. It has been shown that the diameter of the semicircle is related to the charge transfer resistance (R_{ct}) and the slope in the low-frequency region is related to the Warburg impedance (Z_w). In the equivalent circuit, R_s corresponds to the contact resistance, R_{ct} is the charge transfer resistance, *CPE* corresponds to the constant phase element, and Z_w is the Warburg impedance (insets in Fig. 4e and Fig. S7). The flexible $MoS_2/C@Ti_3C_2T_x$ electrode has a smaller R_{ct} (38.9 Ω) than $MoS_2@Ti_3C_2T_x$ (74.65 Ω),

suggesting that addition of PVP-derived carbon enhances the charge transfer ability [45]. In addition, the large slope indicates large lithium-ion diffusion rates as a result of the larger interlayer distance.

To detect the electrochemical kinetics of the flexible MoS_2/C@$Ti_3C_2T_x$ electrode, CV is performed at scanning rates from 0.1 to 1 mV s^{-1} to determine the redox pseudocapacitance contributions (Fig. S8). The relationship between the peak current (i) and scanning rate (v) follows the following power law [46]:

$$i = av^b \tag{2}$$

where b = 0.5 or 1 corresponds to the diffusion-controlled or behavior pseudocapacitive effect, respectively. Figure 4f shows that the b values of the anodic and cathodic peaks are 0.80 and 0.87, respectively, suggesting the surface faradaic redox reaction is predominant in the electrochemical reaction. The ratio of the capacitive contribution is further quantified by Eq. (3) [47]:

$$i = k_1v + k_2v^{1/2} \tag{3}$$

where k_1v is the non-diffusion contribution and $k_2v^{1/2}$ is the diffusion-controlled contribution [48]. As observed in Fig. 4g, with increasing scanning rates, the charge storage rate increases in the surface-controlled process. The pseudocapacitive contribution exhibits an increasing tendency with scanning rates and is 81% for a scanning rate of 1 mV s^{-1} (Fig. 4h). The high pseudocapacitive contribution of the MoS_2/C@$Ti_3C_2T_x$ composite mainly originates from the PVP-derived carbon, which can provide more active redox sites for the pseudocapacitive behavior [49]. The results indicate that a large high pseudocapacitive contribution is crucial to the electron transport kinetics.

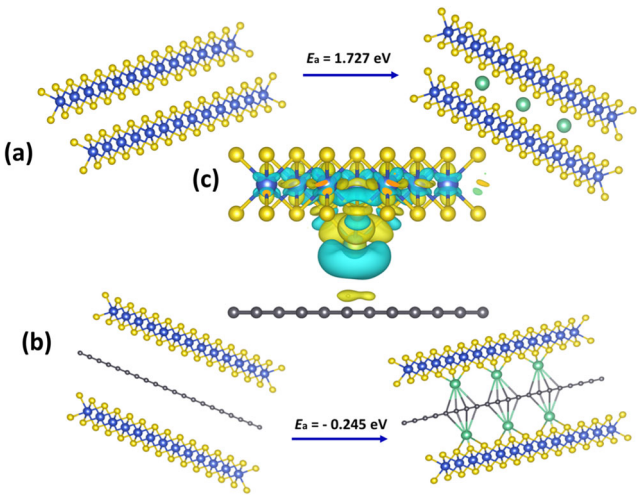

Fig. 5 Lithium adsorption in **a** MoS_2/MoS_2 and **b** MoS_2/C/MoS_2 interlayer. **c** Charge density of Li adsorption in MoS_2/C interface. Yellow and turquoise regions indicate the accumulation and depletion, respectively

Since the PVP-derived carbon increases the interlayer distance of MoS_2, the Li^+ storage mechanism is determined by DFT calculation of MoS_2/C [50, 51] in which the carbon layer is graphene. As shown in Fig. 5a and b, MoS_2/C exhibits stronger chemical adsorption with lower binding energies (E_a = − 0.245 eV) than MoS_2 which shows weaker physical adsorption with a larger binding energy (E_a = 1.727 eV) (Table S3). Therefore, the PVP-derived carbon enhances adsorption of Li^+ due to the larger negative adsorption energy and better charge transfer [34, 52]. To further study the electronic structure of MoS_2/C, the charge density is analyzed as shown in Fig. 5c. Charge exchange occurs between the PVP-derived carbon and MoS_2, and charges are mainly lost from Li to accumulate in the Li-S and Li-C bonds. In this way, the intercalated PVP-derived carbon (graphene in this model) creates a stable channel for Li^+ transport consequently improving charge transport.

Conclusions

The flexible sandwiched structure consisting of rice-candy-like MoS_2/C nanosheets intercalated in $Ti_3C_2T_x$ is designed and demonstrated as high-performance electrode materials in Li-ion batteries. The large interlayer spacing provides abundant and rapid diffusion channels for the electrolyte and there are more adsorption sites to enhance the electrochemical characteristics. The PVP-derived carbon layer enhances the electrical conductivity and structural robustness. As a demonstration of the commercial viability in Li-ion batteries, the flexible MoS_2/C@$Ti_3C_2T_x$ anode exhibits remarkable reversible capacities and coulombic efficiency, improved rate performance, and outstanding cycling stability. DFT calculation reveals that lithium storage on the MoS_2/C nanosheets leads to more intercalation to enhance adsorption/diffusion of lithium ions. The flexible MoS_2/C@$Ti_3C_2T_x$ electrode has large commercial potential, and the design and fabrication strategy provide insights into the development of superior electrochemical properties for flexible energy storage equipment.

Supplementary Information The online version contains supplementary material available at https://doi.org/10.1007/s10008-021-04936-8.

Funding This work was financially supported by the National Natural Science Foundation of China (Nos. 61574122 and 61874093), Zhongyuan Thousand Talents Plan - Science & Technology Innovation Leading Talents Project (No. 194200510009), Key Scientific Research Projects of Higher Education Institutions in Henan Province (19A430023), and the Nanhu Scholars Program for Young Scholars of XYNU, Xinyang Normal University Analysis & Testing Center, and City University of Hong Kong Strategic Research Grant (SRG) (No. 7005505).

Declarations

Conflict of interest The authors declare no competing interests.

References

1. Wang YJ, Zhen MM, Liu HL, Wang C (2018) Interlayer-expanded MoS_2/graphene composites as anode materials for high-performance lithium-ion batteries. J Solid State Electrochem 22(10):3069–3076
2. Hu ZL, Kuai XX, Chen JT, Sun PT, Zhang QB, Wu HH, Zhang L (2020) Strongly coupled MoS_2 nanocrystal/Ti_3C_2 nanosheet hybrids enable high-capacity lithium-ion storage. ChemSusChem 13(6):1485–1490
3. Sen UK, Mitra S (2014) Improved electrode fabrication method to enhance performance and stability of MoS_2-based lithium-ion battery anode. J Solid State Electrochem 18(10):2701–2708
4. Chen X, Berner NC, Backes C, Duesberg GS, McDonald AR (2016) Functionalization of two-dimensional MoS_2 on the reaction between MoS_2 and organic thiols. Angew Chem Int Ed 55(19): 5803–5808
5. Ma XX, Li N, Liu SK, Zhang K, Chi CX, Zhao JP, Liu XX, Li Y (2018) Pyrrolic nitrogen-doped carbon sandwiched monolayer MoS_2 vertically anchored on graphene oxide for high-performance sodium-ion battery anodes. J Solid State Electrochem 22(9):2801–2809
6. Xu GB, Yang LW, Wei XL, Ding JW, Zhong JX, Chu PK (2016) MoS_2-Quantum-dot-interspersed $Li_4Ti_5O_{12}$ nanosheets with enhanced performance for Li- and Na-ion batteries. Adv Funct Mater 26(19):3349–3358
7. Ali GAM, Thalji MR, Soh WC, Algarni H, Chong KF (2020) One-step electrochemical synthesis of MoS_2/graphene composite for supercapacitor application. J Solid State Electrochem 24(1):25–34
8. Song XH, Chen QB, Shen EH, Liu HL (2019) Supercapacitive performances of few-layer MoS2 on reduced graphene oxides. J Solid State Electrochem 23(3):911–923
9. Jiang Y, Guo YB, Lu WJ, Feng ZY, Xi BJ, Kai SS, Zhang JZ, Feng JK, Xiong SL (2017) Rationally incorporated MoS_2/SnS_2 nanoparticles on graphene sheets for lithium-ion and sodium-ion batteries. ACS Appl Mater Interfaces 9(33):27697–27706
10. Li ZY, Fan RY, Hu Z, Li WC, Zhou HJ, Kang SH, Zhang YX, Zhang HM, Wang GZ (2020) Ethanol introduced synthesis of ultrastable 1T-MoS_2 for removal of Cr (VI). J Hazard Mater 394: 122525
11. Zhu ZQ, Tang YX, Lv ZS, Wei JQ, Zhang YY, Wang RH, Zhang W, Xia HR, Ge MZ, Chen XD (2018) Fluoroethylene carbonate enabling a robust LiF-rich solid electrolyte interphase to enhance the stability of the MoS_2 anode for lithium-ion storage. Angew Chem Int Ed 57(14):3656–3660
12. Yao ZR, Zhu KJ, Li X, Wang J, Yan K, Liu JS (2020) Interlayer-expanded MoS_2 nanosheets/nitrogen-doped carbon as a high-performance anode for sodium-ion batteries. J Alloys Compd 838:155541
13. Sun HH, Wang J-G, Zhang Y, Hua W, Li YY, Liu HY (2018) Ultrafast lithium energy storage enabled by interfacial constructing interlayer-expanded MoS_2 /N-doped carbon nanowires. J Mater Chem A 6(27):13419–13427
14. Zhang YL, Mu ZJ, Yang C, Xu ZK, Zhang S, Zhang XY, Li YJ, Lai JP, Sun ZH, Yang Y, Chao YG, Li CJ, Ge XX, Yang WX, Guo SJ (2018) Rational design of MXene/1T-2H MoS_2-C nanohybrids for high-performance lithium–sulfur batteries. Adv Funct Mater 28(38):1707578
15. Ji YJ, Wei QL, Sun YG (2018) Superior capacitive performance enabled by edge-oriented and interlayer-expanded MoS_2 nanosheets anchored on reduced graphene oxide sheets. Ind Eng Chem Res 57(13):4571–4576
16. Ning MQ, Man QK, Tan GG, Lei ZK, Li JB, Li R-W (2020) Ultrathin MoS_2 nanosheets encapsulated in hollow carbon spheres: a case of a dielectric absorber with optimized impedance for efficient microwave absorption. ACS Appl Mater Interfaces 12(18): 20785–20796
17. Xu X, Zhao RS, Ai W, Chen B, Du HF, Wu LS, Zhang H, Huang W, Yu T (2018) Controllable design of MoS_2 nanosheets anchored on nitrogen-doped graphene: toward fast sodium storage by tunable pseudocapacitance. Adv Mater 30(27):1800658
18. Dong XY, Xing Z, Zheng GJ, Gao XR, Hong HP, Ju ZC, Zhuang QC (2020) MoS_2/N-Doped graphene aerogels composite anode for high performance sodium/potassium ion batteries. Electrochim Acta 339:135932
19. Guan XB, Zhao LP, Zhang PL, Liu J, Song XF, Gao L (2020) Electrode material of core-shell hybrid MoS_2@C/CNTs with carbon intercalated few-layer MoS_2 nanosheets. Mater Today Energy 16:100379
20. Yang XD, Yang YB, Fu LN, Zou MC, Li ZH, Cao AY, Yuan Q (2018) An ultrathin flexible 2D membrane based on single-walled nanotube–MoS_2 hybrid film for high-performance solar steam generation. Adv Funct Mater 28(3):1704505
21. Wu P-R, Zhang W, Liu Z, Cheng Z-L (2019) A novel preparation method for MoS_2 nanosheets with good tribology performance by the combination of expansion and freeze exfoliation. Ceram Int 45(2):1730–1736
22. Sun HH, Liu HY, Hou ZD, Zhou R, Liu XR, Wang J-G (2020) Edge-terminated MoS_2 nanosheets with an expanded interlayer spacing on graphene to boost supercapacitive performance. Chem Eng J 387:124204
23. Wang G, Zhang J, Yang S, Wang FX, Zhuang XD, Müllen K, Feng XL (2017) Vertically aligned MoS_2 nanosheets patterned on electrochemically exfoliated graphene for high-performance lithium and sodium storage. Adv Energy Mater 8:1702254
24. Jing Y, Ortiz-Quiles EO, Cabrera CR, Chen ZF, Zhou Z (2014) Layer-by-layer hybrids of MoS_2 and reduced graphene oxide for lithium-ion batteries. Electrochim Acta 147:392–400
25. Wu X, Wang Z, Yu M, Xiu L, Qiu J (2017) Stabilizing the MXenes by carbon nanoplating for developing hierarchical nanohybrids with efficient lithium storage and hydrogen evolution capability. Adv Mater 29(24):1607017
26. Wang WX, Lu Y, Zhao ML, Luo RJ, Yang Y, Peng T, Yan HL, Liu XM, Luo YS (2019) Controllable tuning of cobalt nickel-layered double hydroxide arrays as multifunctional electrodes for flexible supercapattery device and oxygen evolution reaction. ACS Nano 13(10):12206–12218
27. Medetalibeyoglu H, Beytur M, Akyıldırım O, Atar N, Yola ML (2020) Validated electrochemical immunosensor for ultrasensitive procalcitonin detection: carbon electrode modified with gold nanoparticles functionalized sulfur doped MXene as sensor platform and carboxylated graphitic carbon nitride as signal amplification. Sensors Actuators B Chem 319:128195
28. Kadirsoy S, Atar N, Yola ML (2020) Molecularly imprinted QCM sensor based on delaminated MXene for chlorpyrifos detection and QCM sensor validation. New J Chem 44(16):6524–6532
29. Özcan N, Medetalibeyoglu H, Akyıldırım O, Atar N, Yola ML (2020) Electrochemical detection of amyloid-β protein by delaminated titanium carbide MXene/multi-walled carbon nanotubes composite with molecularly imprinted polymer. Mater Today Commun 23:101097
30. Chen X, Wang SL, Shi JJ, Du XY, Cheng QH, Xue R, Wang Q, Wang M, Ruan LM, Zeng W (2019) Direct laser etching free-

standing MXene-MoS_2 film for highly flexible micro-supercapacitor. Adv Mater Interfaces 6(22):1901160
31. Yu P, Cao GJ, Yi S, Zhang X, Li C, Sun XZ, Wang K, Ma YW (2018) Binder-free 2D titanium carbide (MXene)/carbon nanotube composites for high-performance lithium-ion capacitors. Nanoscale 10(13):5906–5913
32. Wu CL, Zhao GY, Gong S, Zhang NQ, Sun KN (2019) A PVP incorporated MoS_2 as Mg ion host with enhanced capacity and durability. J Mater Chem A 7(9):4426–4430
33. Wang YH, Yang Y, Zhang DY, Wang YB, Luo XK, Liu XM, Kim J-K, Luo YS (2020) Inter-overlapped MoS_2/C composites with large-interlayer -spacing for high-performance sodium-ion batteries. Nanoscale Horiz 5(7):1127–1135
34. Deng ZN, Jiang H, Hu YJ, Liu Y, Zhang L, Liu HL, Li C (2017) 3D ordered macroporous MoS_2@C nanostructure for flexible Li-ion batteries. Adv Mater 29(10):1603020
35. Ding L, Wei YY, Wang YJ, Chen HB, Caro JG, Wang HH (2017) A Two-dimensional lamellar membrane: MXene nanosheet stacks. Angew Chem Int Ed 56(7):1825–1829
36. Fu JJ, Yun JM, Wu SX, Li LL, Yu LT, Kim K (2018) Architecturally robust graphene-encapsulated MXene Ti_2CT_x@Polyaniline composite for high-performance pouch-type asymmetric supercapacitor. ACS Appl Mater Interfaces 10(40): 34212–34221
37. Su TM, Hood ZD, Naguib M, Bai L, Luo S, Rouleau CM, Ivanov IN, Ji HB, Qin ZZ, Wu ZL (2019) Monolayer $Ti_3C_2T_x$ as an effective co-catalyst for enhanced photocatalytic hydrogen production over TiO_2. ACS Appl Energy Mater 2(7):4640–4651
38. Pan ZH, Cao F, Hu X, Ji XH (2019) Facile CuS decorated Ti_3C_2 MXene with enhanced performance for asymmetric supercapacitor. J Mater Chem A 7(15):8984–8992
39. Liu J, Zhang H-B, Sun RH, Liu YF, Liu ZS, Zhou A, Yu Z-Z (2017) Hydrophobic, flexible, and lightweight MXene foams for high-performance electromagnetic-interference shielding. Adv Mater 29(38):1702367
40. Yan J, Ren CE, Maleski K, Hatter CB, Anasori BA, Urbankowski P, Sarycheva A, Gogotsi Y (2017) Flexible MXene/graphene films for ultrafast supercapacitors with outstanding volumetric capacitance. Adv Funct Mater 27(30):1701264
41. Zhao Z-H, Hu X-D, Wang HQ, Ye M-Y, Sang Z-Y, Ji H-M, Li X-L, Dai Y (2018) Superelastic 3D few-layer MoS_2/carbon framework heterogeneous electrodes for highly reversible sodium-ion batteries. Nano Energy 48:526–535
42. Ma K, Jiang H, Hu YJ, Li CZ (2018) 2D Nanospace confined synthesis of pseudocapacitance-dominated MoS_2-in-Ti_3C_2 superstructure for ultrafast and stable Li/Na-ion batteries. Adv Funct Mater 28(40):1804306
43. Xie XQ, Makaryan T, Zhao MQ, Van Aken KL, Gogotsi Y, Wang GX (2016) MoS_2 nanosheets vertically aligned on carbon paper: a freestanding electrode for highly reversible sodium-ion batteries. Adv Energy Mater 6(5):1502161
44. Wang J-G, Liu HY, Zhou R, Liu XG, Wei BW (2019) Onion-like nanospheres organized by carbon encapsulated few-layer MoS_2 nanosheets with enhanced lithium storage performance. J Power Sources 413:327–333
45. Lei ZD, Xu LQ, Jiao YL, Du AJ, Zhang Y, Zhang HJ (2018) Strong coupling of MoS_2 nanosheets and nitrogen-doped graphene for high-performance pseudocapacitance lithium storage. Small 14(25):1704410
46. Chao YF, Jalili RH, Ge Y, Wang CY, Zheng T, Shu KW, Wallace GG (2017) self-assembly of flexible free-standing 3D porous MoS_2-reduced graphene oxide structure for high-performance lithium-ion batteries. Adv Funct Mater 27:1700234
47. Bai J, Zhao BC, Lin S, Li KZ, Zhou JF, Dai JM, Zhu XB, Sun YP (2020) Construction of hierarchical V_4C_3-MXene/MoS_2/C nanohybrids for high-rate lithium-ion batteries. Nanoscale 12(2): 1144–1154
48. Huang HW, Cui J, Liu GX, Bi R, Zhang L (2019) Carbon coated $MoSe_2$/MXene hybrid nanosheets for superior potassium storage. ACS Nano 13(3):3448–3456
49. Wu YT, Nie P, Jiang JM, Ding B, Dou H, Zhang XG (2017) MoS_2 Nanosheets decorated 2D titanium carbide (MXene) as high-performance anodes for sodium-ion batteries. ChemElectroChem 4(6):1560–1565
50. Veerasubramani GK, Park M-S, Nagaraju G, Kim D-W (2019) Unraveling the Na-ion storage performance of a vertically aligned interlayer-expanded two-dimensional MoS_2@C@MoS_2 heterostructure. J Mater Chem A 7(42):24557–24568
51. Chen C, Xie X, Anasori B, Sarycheva A, Makaryan T, Zhao MQ, Urbankowski P, Miao L, Jiang JJ, Gogotsi Y (2018) MoS_2-on-MXene heterostructures as highly reversible anode materials for lithium-ion batteries. Angew Chem Int Ed 57(7):1846–1850
52. Xie XQ, Ao ZM, Su DW, Zhang JQ, Wang GX (2015) MoS_2/graphene composite anodes with enhanced performance for sodium-ion batteries: the role of the two-dimensional heterointerface. Adv Funct Mater 4:1393–1403